Improved quantification of ocean carbon uptake by using machine learning to merge global models and pCO_2 data

L. Gloege[1], and M. Yan[2], and T. Zheng[2,3], and G. A. McKinley[4]

[1]Department of Earth and Environmental Engineering, Columbia University, New York, NY 10027, USA
[2]Data Science Institute, Columbia University, New York, NY 10027, USA
[3]Department of Statistics, Columbia University, New York, NY 10027, USA
[4]Lamont-Doherty Earth Observatory and Department of Earth and Environmental Sciences, Columbia University, New York, NY 10027, USA

Key Points:

- LDEO-HPD is in better agreement with independent data than existing products
- LDEO-HPD ocean uptake of CO_2 is in agreement with other products as well as the Global Carbon Budget 2020 for the last decades
- LDEO-HPD can be used as a diagnostic tool to evaluate spatio-temporal model fields

Corresponding author: Lucas Gloege, ljg2157@columbia.edu

Abstract

The ocean plays a critical role in modulating climate change by sequestering CO_2 from the atmosphere. Quantifying the CO_2 flux across the air-sea interface requires time-dependent maps of surface ocean partial pressure of CO_2 (pCO_2), which can be estimated using global ocean biogeochemical models (GOBMs) and observational-based data products. GOBMs are internally consistent, mechanistic representations of the ocean circulation and carbon cycle, and have long been the standard for making spatio-temporally resolved estimates of air-sea CO_2 fluxes. However, there are concerns about the fidelity of GOBM flux estimates. Observation-based products have the strength of being data-based, but the underlying data are sparse and require significant extrapolation to create global full-coverage flux estimates. The Lamont Doherty Earth Observatory-Hybrid Physics Data (LDEO-HPD) pCO_2 product is a new approach to estimating the temporal evolution of surface ocean pCO_2 and air-sea CO_2 exchange. LDEO-HPD uses machine learning to merge high-quality observations with state-of-the-art GOBMs. We train an eXtreme Gradient Boosting (XGB) algorithm to learn a non-linear relationship between model-data mismatch and observed predictors. GOBM fields are then corrected with the predicted model-data misfit to estimate real-world pCO_2 for 1982-2018. A benefit of this approach is that model-data misfit has reduced temporal skewness compared to the observed pCO_2 that is the target variable for other machine-learning based reconstructions. This supports a robust reconstruction by LDEO-HPD that is in better agreement with independent observations than other estimates. LDEO-HPD global ocean uptake of CO_2 is in agreement with other products and the Global Carbon Budget 2020.

Plain Language Summary

The ocean absorbs carbon from the atmosphere, which slows climate change. In order to estimate how much carbon the ocean absorbs, we need to know how much is exchanged from the atmosphere into the ocean at each location over time. The direct observations required to do this are very sparse and in some regions of the ocean, observations have never been made. One approach to fill in the gaps is to use machine-learning, which are algorithms that build a relationship for ocean carbon based on related satellite observations with global coverage. Another approach is to use computer simulations, which use mathematical equations to represent ocean processes. Here, we merge these two innovations by blending model output with machine-learning to create a hybrid product: the Lamont Doherty Earth Observatory-Hybrid Physics Data (LDEO-HPD). Particularly for the most recent decade, LDEO-HPD agrees slightly better with independent observations than other products, indicating the promise of this approach.

1 Introduction

The ocean's net uptake of CO_2 is a key component of the global carbon cycle. Quantifying how anthropogenic emissions are distributed between atmosphere, land biosphere, and ocean reservoirs with as low uncertainty as possible is needed to support international climate policy (Peters et al., 2017). The Global Carbon Budget 2020 (Friedlingstein et al., 2020) finds that for 2009-2018, the ocean sink for anthropogenic carbon was -2.5 $\pm$ 0.6 PgC/yr (negative flux into the ocean), based on global ocean biogeochemical models (GOBMs). However, four observation-based products suggest a sink that is 0.4 PgC/yr larger for this period. Do the relatively-new observation-based estimates indicate a serious problem with the long-used GOBMs? Do they require fundamental change in understanding of how carbon sinks in the ocean and on land are evolving?

Estimating the global ocean CO_2 sink requires knowledge of ocean partial pressure of CO_2 (pCO_2). The Surface Ocean CO_2 ATlas (SOCAT) is an annually compiled database of surface ocean fugacity of CO_2 (fCO_2) with over 28.2 million observations for 1957-2019 in the SOCATv2020 release (Bakker et al., 2016), mainly from volunteer observing ships.

fCO_2 is nearly equivalent to pCO_2, different by a 0.3% non-ideality correction; we make this adjustment in our analysis to derive pCO_2 (Section 2.1). Due to limited number of ships, routes, and the high cost of maintenance, the data retrieved from this observation system remains sparse in space and time. Data are concentrated in the Northern Hemisphere (Figure 1A,B,C). Using these data alone, pCO_2 cannot be quantified at all times and all locations, and thus statistical extrapolations have been performed to create observation-based data products (Rödenbeck et al., 2015). The carbon cycle community uses these products along with global ocean biogeochemical models (GOBMs) (Friedlingstein et al., 2020) to independently estimate CO_2 fluxes and, through their analysis and comparison, to improve knowledge of the global ocean carbon cycle. We propose an explicit merging of the strengths of both approaches in the form of a hybrid observation-based data product that uses pCO_2 estimates from multiple GOBMs as a prior.

A GOBM is a knowledge-based model that parameterizes the physical, chemical, and biological processes influencing surface ocean pCO_2 using a system of coupled differential equations. GOBMs have long been taken as the best estimate of the anthropogenic air-sea CO_2 flux, and have always been the basis for quantification of the ocean carbon sink in the annual Global Carbon Budget published by the Global Carbon Project since 2009 (Le Quéré et al., 2009; Friedlingstein et al., 2020). Nine GOBMs were used as the basis for the Global Carbon Budget in 2019 and 2020 (Friedlingstein et al., 2019, 2020). These models are certainly imperfect, with substantial differences among them and potentially an underestimation of CO_2 flux variability, particularly in the Southern Ocean (Gruber, Landschützer, & Lovenduski, 2019; Hauck et al., 2020; Gloege et al., 2021). However, based on a long history of their application to understanding and quantification of air-sea CO_2 fluxes, it is a sensible to use GOBMs as a prior estimate upon which data-based improvements can be made.

Most observation-based products find a relationship between a suite of datasets and the target variable (ocean pCO_2) using machine learning algorithms. The statistical relationships of the algorithm are dependent on the quantity and quality of SOCAT pCO_2 data, driver data, and the skill of the reconstruction algorithm. A recent assessment of the SOM-FFN (Landschützer et al., 2014) reconstruction indicates high fidelity for the mean and seasonality of pCO_2-based CO_2 flux estimates. However, pCO_2 data sparsity (Figure 1A,B,C) limits the ability to reconstruct interannual to decadal timescale variations (Gloege et al., 2021). Though the spread across the full suite of recently-published products is smaller than the spread across the current generation of models (McKinley et al., 2020), there remain substantial differences in the timing and amplitude of interannual variability (Friedlingstein et al., 2020). In a comprehensive evaluation of multiple products, Gregor et al. (2019) find comparable skill with respect to independent data in the current generation of products, and suggest that we have reached a skill limit for these products that is fundamentally due to data sparsity.

Both GOBMs (Friedlingstein et al., 2020; Hauck et al., 2020) and observation-based products (Rödenbeck et al., 2015) provide approximately global estimates of ocean pCO_2 and CO_2 flux. The two approaches differ significantly in the way they estimate ocean pCO_2. GOBMs compute the evolution of physical and biogeochemical processes based on complex systems of coupled differential equations that can only be solved numerically. Observation-based products do not explicitly incorporate known physics, but instead estimate a non-linear relationship between a handful of driver datasets and ocean pCO_2 where these are co-located. Global full-coverage driver datasets are then processed through these relationships to estimate global full-coverage pCO_2. GOBMs and observation-based data products generally agree on the large-scale patterns and long-term increase in ocean pCO_2 (Tjiputra et al., 2014; Landschützer et al., 2014; McKinley et al., 2016, 2020). For aggregated comparisons over large regions, GOBMs have comparable root mean square errors against SOCAT pCO_2 to those in the observation-based products, indicating comparable skill (Gregor et al., 2019; Hauck et al., 2020). However, GOBMs are biased high

when sub-sampled at SOCAT observation locations (Figure 1D). In some models, this global bias is at least partially attributable to the exclusion of the well-established water vapor correction (Dickson et al., 2007) in the calculation of atmospheric pCO_2 (McKinley et al., 2020).

As noted above, the pCO_2 data required to train machine learning algorithms are spatially sparse (Figure 1A,B,C). Data availability also changes over time (Figure 2A,B). This trend in data availability, combined with the long-term positive trend in ocean pCO_2 ($\sim$33 μatm increase from 1980s to 2010s) has the potential to impact the ability of algorithms to represent the data. Machine learning, or any statistical fit, performs best when target variables distributions have the same shape as the driver variables (Goodfellow et al., 2016). With ocean pCO_2 as the target variable, the algorithm is being asked to predict a broad and right-skewed distribution (Figure 1A) that is unlike the drier variables that do not have a significant temporal shift. In contrast, the difference between observed and GOBM-estimated pCO_2 has only a modest long-term trend ($\sim$9 μatm from 1980s to 2010s, Figure 2C,D). Thus, if we use the difference between SOCAT observations and the GOBMs as a basis for algorithm development, we largely address the aforementioned concern. In other words, with model-data misfit as our target variable, the skewness of the target variable is substantially reduced (Figure 2C).

In this study, we leverage the nine GOBMs used in the Global Carbon Budget 2020 (Friedlingstein et al., 2020) and combine them with a supervised machine learning algorithm to create the LDEO-Hybrid Physics Data ocean pCO_2 observation-based product (LDEO-HPD). Instead of using ocean pCO_2 as the target variable, as do other data products (Landschützer et al., 2014; Rödenbeck et al., 2015; Gregor et al., 2019; Denvil-Sommer et al., 2019), the target variable for our eXtreme Gradient Boosting (XGB) algorithm is the misfit between SOCAT observed pCO_2 and each model where SOCAT observations exist in space and time ($pCO_{2,SOCAT} - pCO_{2,GOBM}$). Our driver data are the same suite of in situ and satellite observations used by other approaches. To make final estimates of actual ocean pCO_2, the XGB algorithm first uses full-field observed driver data to predict model misfit at all locations for each GOBM. These misfit fields are then added back to each GOBM to make the final estimate. Each GOBM is processed using a unique algorithm, and the final LDEO-HPD output is the average of the nine merged data-model estimates. See Figure 3 for a schematic. Our approach of combining data-based machine learning with the physics embodied in dynamical models follows on recent innovations in physics-guided machine learning (Karpatne et al., 2017; Reichstein et al., 2019) and the use of machine learning to correct dynamical models (Watt-Meyer et al., 2021) for earth science applications.

A potential additional application of the approach we develop here is to use model-data misfit fields to visualize and quantify errors in GOBM carbon cycle simulations at broader temporal and spatial scales than is currently possible with actual SOCAT data (Hauck et al., 2020). Spatio-temporal misfit mapped by the algorithm is a direct estimate of GOBM skill for locations where in situ data do not exist. We briefly explore this application in Section 3.1.

2 Methods

GOBM output is incorporated into a supervised machine learning algorithm to create a hybrid data product for 1982-2018. We use gradient boosting as implemented in the eXtreme Gradient Boosting (XGB) library (Chen & Guestrin, 2016). XGB learns a non-linear relationship between a suite of features and the misfit between the GOBM and direct SOCAT observations. We use this approach to upscale SOCAT pCO_2 observations and create a nearly global, temporally complete data product. The upscaled pCO_2 product is statistically evaluated against independent observations and other published data products. A schematic of HPD is shown in Figure 3. From pCO_2 estimated with

HPD, we estimate CO_2 flux using the standard bulk parameterization that relates the flux to wind speed (Wanninkhof, 1992, 2014; Fay et al., 2021).

2.1 Pre-processing SOCAT observations

We use surface ocean pCO_2 calculated from the SOCAT v2019 monthly gridded fCO_2 product. SOCAT v2019 is a quality-controlled dataset that contains observations of surface ocean fCO_2, which is converted to pCO_2 with equation 1,

$$\mathrm{pCO_2} = \mathrm{fCO_2} \cdot \exp\left(P_{\mathrm{atm}}^{\mathrm{surf}} \cdot \frac{B + 2\delta}{R \cdot T}\right)^{-1} \tag{1}$$

where P_{atm}^{surf} is the atmospheric surface pressure from ERA5, T is the sea surface temperature (SST) in Kelvin from National Oceanic and Atmospheric Administration (NOAA) daily optimally interpolated SST version 2 (dOISSTv2), B and δ are virial coefficients from (Weiss, 1974), R is the gas constant (Dickson et al., 2007).

2.2 Global Ocean Biogeochemical Models

As a first guess for ocean pCO_2, we use output from nine GOBMs (Table 1) which participated in the Global Carbon Budget 2020 (Friedlingstein et al., 2020), with the final year being 2018. Meteorological reanalysis and atmospheric CO_2 are used to force each model (Hauck et al., 2020). Each GOBM parameterizes the physical, chemical, and biological processes influencing surface ocean pCO_2 using a system of coupled differential equations. The surface pCO_2 from each GOBM is bi-linearly interpolated from the native model grid to a 1°x1° monthly resolution to be consistent with SOCAT gridded observations (Sabine et al., 2013).

Table 1. Global Ocean Biogeochemical Models

Reference for GOBMs used in the Global Carbon Budget 2020 (Friedlingstein et al., 2020).

Global ocean biogeochemical models (GOBMs)	Reference
NEMO-PlankTOM5	Buitenhuis et al. (2013)
MICOM-HAMOCC (NorESM1-OCv1.2)	Schwinger et al. (2016)
MPIOM-HAMOCC6 (MPI)	Paulsen et al. (2017)
NEMO3.6-PISCESv2-gas (CNRM)	Berthet et al. (2019)
CISRO	Law et al. (2017)
FESCOM-1.4-REcoM2	Hauck et al. (2020)
MOM6-COBALT (princeton)	Adcroft et al. (2019)
CESCM-ETHZ	Doney et al. (2009)
NEMO-PISCES (IPSL)	Aumont et al. (2015)

2.3 Machine learning method and the LDEO-HPD product

Extreme Gradient Boosting (XGB) (Chen & Guestrin, 2016) is a supervised machine learning algorithm where multiple features, X, are used to predict a target variable y. The XGB algorithm can then be used to estimate a function, $f(X)$, such that: $y \approx f(X)$. The algorithm begins with an initial guess for y, a choice to which the algorithm is not sensitive. As illustrated in Figure 3B, a decision tree is used to learn the difference between the training data and the initial guess. This new tree is added to the

initial guess. This process of adding trees to correct the errors made in the summation of previous trees is repeated until either a predefined number of trees has been made, or when adding an additional tree results in no further improvement. The final prediction is the sum of all trees such that the closest fit of input data and algorithm output is achieved. A mean-squared-error (MSE) loss function is minimized using gradient descent.

Gradient boosting algorithm, as implemented in the eXtreme Gradient Boosting (XGB) library version 0.9 with the scikit-learn wrapper (Chen & Guestrin, 2016), is used to find a non-linear relationship between a suite of input features and the misfit between each GOBM and SOCAT pCO_2: ($pCO_{2,SOCAT} - pCO_{2,GOBM}$). This algorithm was chosen because it leads to a better fit to input data than the other options considered, neural network or random forest (Stamell et al., 2020). To estimate pCO_2 at each spatial location, the algorithm relies on datasets with full, or approximately full, global coverage (Table 2): Sea Surface Temperature (SST) and Surface Chlorophyll-a (Chl-a) from satellite; Sea Surface Salinity (SSS) from a compilation of in-situ data sources; Mixed layer depth (MLD) climatology from ARGO floats; and atmospheric CO_2 mixing ratio (xCO_2) from station sites. These variables serve as proxies for known processes affecting pCO_2. Solubility is set by SSS and SST. Biological uptake of dissolved inorganic carbon (DIC) is indicated by Chl-a. Biological productivity and entrainment of DIC are influenced by MLDs. The long-term growth of ocean pCO_2 is driven by atmospheric xCO_2. Additional annual mean anomaly features are derived for SST and Chl-a by subtracting the annual mean from each year. These features help the algorithm learn more complex relationships and capture intra-annual variability. N-vector transformation (Gade, 2010; Sasse et al., 2013; Gregor et al., 2017) of latitude and longitude is included to help the algorithm learn spatial relationships. Time transformation of the day of year constrains seasonality (Gregor et al., 2017).

The features and associated pCO_2 misfit are split into three sets: validation, training, and testing. The validation is used to optimize the algorithms hyperparameters, which defines the architecture of decision trees used in the model. The training set is used to construct the decision trees. The withheld test set is used to evaluate performance on a completely independent dataset, individual years are withheld for the test set to retain individual ship tracks and increase the independence of test data from training and validation data (Gregor et al., 2019).

Our XGB algorithm uses 1500 decision trees each with a max depth of 9 levels or until no further splits to the samples in that node are possible. Each new tree uses 95% of the features and a random subsample of observations with replacement. The weight of each sequential tree is reduced by 5%. Light L1 regularization was applied to control overfitting and loss is measured using mean-squared error (MSE).

XGB is used to estimate spatio-temporal estimates of the misfit for each of nine GOBMs. Misfit estimates at all locations in space and time are added back to the original GOBM to correct the GOBM toward the data. This process is repeated for each of the nine GOBMs. The final result is then the average of all nine predictions. A schematic of HPD is shown in Figure 3.

Table 2. Feature and target datasets

Summary of the products, variables, and data processing steps used for feature and target variables. Data processing is described in the text. Symbol next to each product identifies the source.

Group: product	Variable	Abbreviation	Processing
SOCATv2019*	Partial pressure of ocean CO_2	pCO_2	See section 2.1
NOAA:OISSTv2†	Sea Surface Temperature	SST	-
	SST seasonal anomaly	SST′	SST - annual average
	Sea Ice Fraction	ICE	-
Met Office:EN4‡	Sea Surface Salinity	SSS	-
NOAA:GLOBALVIEW§	Atmospheric CO_2 mixing ratio	xCO_2	-
DeBoyer:Mixed Layer Depth|	Mixed Layer Depth	MLD	$\log_{10}(MLD)$
ESA:GlobColour¶	Chlorophyll-a	Chl a	$\log_{10}(Chla)$
	Chl a seasonal anomaly	Chl a′	chl a - annual average
-	Day of year	J_1	$\sin\left(\frac{j*2\pi}{365}\right)$
		J_2	$\cos\left(\frac{j*2\pi}{365}\right)$
-	n-vector	A	$\sin(\lambda)$
		B	$\sin(\mu)\cos(\lambda)$
		C	$-\cos(\mu)\cos(\lambda)$

∗ Source: https://www.socat.info/

† Source: https://www.esrl.noaa.gov/psd/data/gridded/data.noaa.oisst.v2.html

‡ Source: https://www.metoffice.gov.uk/hadobs/en4/

§ Source: https://www.esrl.noaa.gov/gmd/ccgg/globalview/co2/co2_intro.html

| Source: http://www.ifremer.fr/cerweb/deboyer/mld/home.php

¶ Source: http://www.globcolour.info/

Table 3. Validation datasets

Accuracy of pCO_2 and total number of 1° x1° grid points is shown for each dataset.

Dataset	Accuracy (μatm)	Grid points	Reference
LDEO database version 2018*	$\pm 2.5\ \mu atm$	16161	Takahashi et al. (2019)
GLODAPv2†	$> 12\ \mu atm$ at 400 μatm	5976	Gregor et al. (2019)
BATS†	$4\ \mu atm$ at 400 μatm	246	Bates (2007)
HOT†	$< 7.6\ \mu atm$ at 400 μatm	214	Dore et al. (2009)

∗ pCO_2 measured with pCO_2 equilibrator

† pCO_2 estimated from DIC and TA

2.4 Independent datasets

Observations not included in the SOCAT database are used to validate the method (Table 3). These datasets include the Lamont-Doherty Earth Observatory (LDEO) database, with SOCAT data removed; and GLobal Ocean Data Analysis Project version 2 (GLODAPv2). Two time series sites are also used for validation: Bermuda Atlantic Time-series Study (BATS) and Hawaii Ocean Time-series (HOT). In these datasets, pCO_2 is either directly measured or inferred from observations using carbonate system calculations with inputs of Dissolved Inorganic Carbon (DIC) and Total Alkalinity (TA). The cbsyst package (Hain et al., 2015) is used for carbonate system calculations. For decadal comparisons, timeframes are 1990s (1990-1999), 2000s (2000-2009) and 2010s (2010-2018).

The uncertainty in derived pCO_2 is dependent on the accuracy of the input measurements. For the modern ocean, cbsyst calculations are consistent with the constants of (Lueker et al., 2000), and result in a 1.9% standard deviation in pCO_2 when DIC and TA uncertainties are 2.0 and 4.0 mol kg-1, respectively. For GLODAP, Bockmon and Dickson (2015) suggests an uncertainty of $5\frac{\mu mol}{kg}$ for DIC and TA, thus suggesting an uncertainty greater than 1.9%. Gregor et al. (2019) estimate the uncertainty of GLODAP pCO_2 to be >12 μatm at 400 μatm. Although the measurements have high uncertainty, given the sparsity of the SOCAT database, including GLODAP as a validation dataset outweighs its omission, consistent with previous studies (Gregor et al., 2019; Gregor & Gruber, 2021). At BATS the uncertainty is about 4 μatm (Bates, 2007) while at HOT it is <7.6 μatm (Dore et al., 2009). LDEO pCO_2 has uncertainty of 2.5 μatm (Takahashi et al., 2019).

2.5 Regression metrics

A suite of regression metrics are used to compare the predictions (P) to the observations (O) (Stow et al., 2009). Metrics considered include correlation (r), bias, and root mean squared error (RMSE). Multiple metrics are considered in order to provide a thorough appraisal of each method. Metrics are displayed in a Taylor diagram (Taylor, 2001).

Pearson correlation coefficient (r) measures the tendency of the predicted and observations to vary together, bounded between ,$-1 < r < 1$, with values near 1 indicating that they vary together and -1 indicating an inverse relationship. Correlation is also a measure of how well the phase is captured. Values near 1 and -1 indicate that the predictions and observations are perfectly in or out of phase, respectively. Intermediate values indicate a phase shift between the two signals, with values closer to zero indicating a larger phase shift between signals. The squared correlation r^2, or coefficient of determination, represents the variance explained by the regression. Correlation is defined as the covariance between predictions and observations divided by the product of their standard deviations, $r = \frac{cov(P,O)}{\sigma_P \sigma_O}$, σ_P and σ_O represent the standard deviation of the predictions and observations, respectively.

Bias, average absolute error (AAE), and RMSE each measure the size of discrepancies, with values near zero indicating a close match between predictions and observations. However, each metric has strengths and weaknesses. Bias is simply calculated as the long-term mean difference between predictions and observations ($bias = \overline{P} - \overline{O}$), where overbars represent the temporal mean. Positive and negative bias values indicate predictions that are generally overestimated and underestimated respectively. Thus, bias provides a measure of the direction of discrepancy. However, bias values falling close to zero can be misleading with significant positive offsets at one point in space or time canceling out significant negative offsets elsewhere. RMSE $=\sqrt{\overline{(P-O)^2}}$ measures of the magnitude of discrepancy, but squaring the misfit makes RMSE sensitive to outliers. Alternatively, AAE $=\overline{|P-O|}$ treats each misfit equally, but is a less commonly used met-

ric. We report bias, AAE and RMSE since each one provides a different insight into the goodness-of-fit.

2.6 Area coverage

The LDEO-HPD product covers 89.6% of the total ocean area, leaving out the Arctic and coastal zones. Before estimating the net carbon flux from observation-based products, we use the method of (Fay et al., 2021) to fill spatial gaps in the pCO_2 product with climatology (Landschützer, Laruelle, et al., 2020) plus the global-mean trend. This fills in the 10.4% to create a global gap-free product. Climatological filling lowers global mean pCO_2 from 356 μatm to 352 μatm in the final product. This climatological filling technique (Fay et al., 2021) was also applied to each observational data product to which we compare our results (Table 5).

2.7 Air-sea CO_2 flux

The air-sea CO_2 exchange was calculated using a bulk parameterization (equation 2):

$$F_{CO_2} = k_w S_{CO_2}(1 - f_{ice})(pCO_2^{atm-moist} - pCO_2^{ocean}) \tag{2}$$

which parameterizes the air-sea CO_2 flux (F_{CO_2}) as a function of the gas transfer velocity (k_w), CO_2 solubility (S_{CO_2}), ice fraction (f_{ice}), and partial pressure of CO_2 in moist air ($pCO_2^{atm-moist}$) and surface ocean (pCO_2^{ocean}). Solubility is calculated following Weiss (1974) and partial pressure of moist air ($pCO_2^{atm-moist}$) is calculated following equation 3,

$$pCO_2^{atm-moist} = xCO_2(P_{atm} - pH_2O) \tag{3}$$

where xCO_2 is the dry air mixing ratio of atmospheric CO_2, P_{atm} is the total atmospheric pressure, and pH_20 is the saturation vapor pressure (Dickson et al., 2007). We use the Wanninkhof (1992) formulation for the gas transfer velocity (equation 4):

$$k_w = k_{w,scaled} u^2 \left(\frac{Sc}{660}\right)^{-0.5} \tag{4}$$

which paramterizes k_w as a function of wind speed squared (u^2) and the Schmidt number (Sc). k_w is scaled by a factor of $k_{w,scaled}$ for each wind product to match the invasion of bomb ^{14}C (Fay et al., 2021). Three wind products were used (Table 4). Flux was calculated separately for each wind product and then averaged to create the final best estimate.

pCO_2 measured in situ and compiled in the SOCAT database is set by the combination of the anthropogenic and natural background carbon cycles. Thus, the calculated flux is the net, or contemporary, flux (F_{NET}).

Table 4. Wind speed products used to calculate CO_2 flux

Wind speed product	Reference
CCMPv2.0*	Mears et al. (2019)
ERA5†	Hersbach et al. (2020)
JRA-55‡	Harada et al. (2016)

∗ Source: `http://www.remss.com/measurements/ccmp/`

† Source: `https://www.ecmwf.int/en/forecasts/datasets/reanalysis-datasets/era5`

‡ Source: `https://jra.kishou.go.jp/JRA-55/`

2.8 Estimating anthropogenic carbon flux from the net flux

The net CO_2 flux is the sum of an anthropogenic and a natural component (F_{NET} = F_{NAT} + F_{ANT}). Surface ocean pCO_2 quantifies F_{NET}, while interior ocean data quantify F_{ANT}. Closure terms are required to compare these independent quantifications of the ocean carbon sink.

The dominant net air-sea flux due to the natural carbon cycle is the outgassing of riverine carbon fluxed into the ocean and then slowly outgassed by the ocean (Aumont et al., 2001). The community's estimate of the net riverine-induced carbon outgassing (F_{RIV}) is still evolving. Here we use an average of three estimates representing the spread of the available approaches: a geochemical budgeting perspective (+0.45 ± 0.18 PgC/yr; Jacobson et al. (2007)), a meridional heat constraint approach (+0.78 ± 0.41 PgC/yr; Resplandy et al. (2018)), and a process-based ocean model (+0.23 PgC/yr; Lacroix et al. (2020)). Since no uncertainty is presented for the Lacroix et al. (2020) estimate, we assume a 50% 1σ uncertainty, which is consistent with the relative magnitude of uncertainty for the other two estimates. Combining these three estimates, we derive an estimate of carbon efflux due to river inpus to the ocean in the observation-based product flux estimates of +0.49 ± 0.26 PgC/yr. This $F_{RIV} \approx F_{NAT}$ will be removed from F_{NET} estimates from HPD and other products to arrive at F_{ANT}.

Watson et al. (2020) propose significant adjustments to SOCAT data to account for a cool and salty near-surface ocean; this adjustment would drive a large increase in F_{NET}. This remains controversial and requires more study. We do not include this adjustment.

Anthropogenic carbon accumulation can be estimated from interior ocean observations, for which a global survey is completed approximately once per decade, and thus this component is estimated over a defined time period. Gruber, Clement, et al. (2019) find F_{ANT} at -2.6 ± 0.3 PgC/yr for 1994-2007. A changing ocean circulation may have modified F_{NAT} over 1994-2007 through a non-steady state outgassing flux of natural carbon. Thus, a natural non-steady state flux ($F_{NAT,NS}$) has been proposed (Gruber, Clement, et al., 2019), i.e. $F_{NAT} = F_{NAT,NS} + F_{RIV}$. Applying the transient steady state assumption to F_{NET} from one observation-based product (Landschützer et al., 2016), Gruber, Clement, et al. (2019) find $F_{NAT,NS}$ =+0.38 PgC/yr. However, the transient steady state assumption is known to hold when atmospheric carbon accumulation is exponential, and this has not been the case in recent decades (Raupach et al., 2014; Ridge & McKinley, 2020). This estimate of $F_{NAT,NS}$ is likely an upper bound. Nevertheless, we follow Gruber, Clement, et al. (2019) and adjust their F_{ANT} estimate by this amount.

Adjusting the F_{ANT} estimate of Gruber, Clement, et al. (2019) leads to F_{ANT} + $F_{NAT,NS}$ = -2.2 ± 0.3 PgC/yr for 1994-2007. Earlier, for the IPCC AR4, Denman et al. (2007) synthesized multiple estimates from ocean and atmosphere tracer studies to estimate F_{ANT} = -2.2 ± 0.4 PgC/yr for 1990-1999, and without any adjustment for $F_{NAT,NS}$. We compare estimate of F_{NET} - F_{RIV} from LDEO-HPD and other products (Table 5) to these estimates.

2.9 Observational-based products

We compare the pCO_2 error statistics and CO_2 flux estimates to four products that extrapolate from SOCAT data to global coverage using machine learning or other statistical modeling techniques (Table 5).

Table 5. Observational data products for comparison to these results

Observation-based pCO_2 product	Reference
MPI-SOMFFN	Landschützer et al. (2014); Landschützer, Gruber, and Bakker (2020)
JENA-MLS	Rödenbeck et al. (2014)
CMEMS	Denvil-Sommer et al. (2019)
CSIR	Gregor et al. (2019)

3 Results

With LDEO-HPD, an XGB algorithm estimates time-varying maps of model-data misfit, and these misfits are then used to adjust model fields to arrive at an estimate of the real-world pCO_2, from which CO_2 flux is then calculated. By identifying large-scale patterns of model mismatch with observations (section 3.1), LDEO-HPD approach reconstructs real-world pCO_2 with greater fidelity than other recently-published approaches (section 3.2). After correcting for riverine outgassing, air-sea CO_2 flux estimates from LDEO-HPD are consistent with independent observations for both 1990-1999 and 1994-2007 (section 3.3).

3.1 Model-data misfit

The 9-model, global-mean bias of 10 μatm in ocean pCO_2 (Figure 1D) can partially be attributed to neglecting to account for the water vapor correction when calculating the atmospheric pCO_2 that forces the model (Dickson et al., 2007). If the molar concentration of CO_2 is measured in dry air then, by standard protocol (Orr et al., 2017), the atmospheric partial pressure of CO_2 must be reduced by the vapor pressure of water (equation 5):

$$pCO_{2,atm} = xCO_2(P - VP_{H20})) \tag{5}$$

where $pCO_{2,atm}$ is the partial pressure of CO_2 in atmosphere, xCO_2 the molar concentration of CO_2 in dry air, P is atmospheric pressure in wet air, and VP_{H20} is vapor pressure of water. This is typically a small percentage correction, but still a change in the pressure field of only 3% changes the partial pressure of CO_2 by about 10 μatm. Thus, if the water vapor correction is ignored, the partial pressure of CO_2 in the atmosphere that the ocean model experiences will be too high and ocean pCO_2 will also be high. Of the nine models, three do not account for this correction, and the other six do (Friedlingstein et al., 2020). Hauck et al. (2020) illustrate through comparison to SOCAT data that these models have a significant high bias in pCO_2. In addition, they show that several models that do include the water vapor correction also have a high pCO_2 bias, but do not identify the source of this error. The mean pCO_2 bias of +10 μatm that we find (Figure 1D) is thus partially, but not fully, attributable to several models not applying the water vapor correction.

The model corrections solved for by the XGB algorithm has significant spatial structure, and thus is doing far more than just addressing a global-mean bias in the GOBM priors. This is illustrated for two of the nine models in Figure 4. There are distinct patterns and consistent seasonality in the required corrections. For the MPI model, in the Southern Ocean and North Pacific, pCO_2 is far too high in winter (JJA) and far to low in summer (DJF), thus the XGB algorithm imposes strong negative and positive corrections, respectively. In the North Atlantic, however, winter is too low and summer is too high, requiring the opposite sign of corrections. In the subtropics, MPI requires a strong negative correction. For CNRM, these patterns are different, with the whole of the winter hemisphere generally being slightly too low in pCO_2 and the majority of the summer hemisphere being too high in pCO_2, requiring modest positive and negative cor-

rection, respectively. Both models require a positive correction in the equatorial Pacific. Zonal-average misfits (Figure 4B) indicate that both of these model require the same sign and comparable magnitude seasonal correction in the extratropical Northern Hemisphere, while MPI requires much larger corrections in the Southern Ocean.

The seasonality of model-data misfits (Figure 4) indicate that the LDEO-HPD is correcting for errors in model representation of seasonal physical and biogeochemical processes, such as mixed layer deepening and biological processes. These machine-learning derived maps of model-data misfit could be applied as a diagnostic of model performance to offer a larger-scale perspective that complements direct comparison to in situ data (Hauck et al., 2020). Model development could be supported with this approach to model-data comparison.

3.2 Evaluation of LDEO-HPD against independent datasets

At the ocean timeseries sites at Bermuda (BATS) and Hawaii (HOT), LDEO-HPD compares quite favorably to the observations. The amplitude of seasonal and interannual variablity in LDEO-HPD is as observed at HOT (Figure 5B, 6A) and slightly underestimated at BATS (Figure 5C, 6B), and the trends at both timeseries are well-represented. Compared to existing pCO_2 gap-filling methods, LDEO-HPD performs slightly better at BATS and HOT, with the lowest unbiased-RMSE relative to SOMFFN, MLS, and CMEMS (Figure 6A,B). Correlations are high at HOT and BATS because of the pronounced subtropical seasonality captured in the datasets. All these products are reliably able to capture subtropical seasonality (Rödenbeck et al., 2015; Gloege et al., 2021; Stamell et al., 2020).

LDEO and GLODAP are global observation datasets from intermittent ship transects. In these data, seasonality is less well-resolved, a fact that helps to explain the lower correlations of all products to the data. All the products show similar performance on LDEO observations, with all the products underestimating the variability (Figure 6C). For comparison to GLODAP, LDEO-HPD has a smaller unbiased-RMSE relative to other products (Figure 6D). LDEO-HPD and MLS capture the amplitude of variability in GLODAP equally well, and slightly better than SOMFFN and CMEMS.

Over time, the skill of LDEO-HPD against independent observations of LDEO and GLODAP increases relative to the other methods. In the 1990s, the skill of all methods are indistinguishable (Figure 7, left). In the 2000s, comparison to GLODAP indicates that LDEO-HPD is slightly better than the others, though there is no distinction across the methonds for LDEO (Figure 7, center). In the 2010s, LDEO-HPD clearly does the best job at capturing GLODAP, and is slightly improved against LDEO (Figure 7, right). Thus, we attribute long-term finding of a better fit to independent observations (Figure 6) is attributable to the better fit of LDEO-HPD in the later decades (Figure 7).

3.3 CO_2 fluxes: 1982-2018

Mean pCO_2 and CO_2 flux from LDEO-HPD algorithm for 1982-2018 show well known features. Elevated pCO_2 is observed at the equator (Figure 8A), especially in the east-equatorial Pacific. This elevated pCO_2 is the result of upwelling of cold, carbon laden waters. The surface pCO_2 in this region is greater than the atmosphere, resulting in net CO_2 flux from the ocean to the atmosphere (Figure 8B).

Over time, the net global CO_2 flux has become increasingly negative (Table 6), i.e. the ocean has become a greater net carbon sink over the recent decades as atmospheric pCO_2 has risen. Coastal filling (Section 2.6) increases uptake by nearly 0.1 to 0.2 PgC/yr, consistent with past estimates of globally integrated coastal uptake (Roobaert et al., 2019).

Table 6. Decadal net CO_2 flux (F_{NET}) (PgC/yr)
CO_2 flux from LDEO-HPD across decades without coastal filling ("unfilled") and filled with the climatology (section 2.6).

	Unfilled	**Filled**
1982-1990	-1.38	-1.53
1990-2000	-1.48	-1.65
2000-2010	-1.49	-1.69
2010-2018	-1.96	-2.23

Applying the same to the calculation of air-sea CO_2 fluxes for all products (Section 2.7), and applying the F_{RIV} correction, we find that fluxes estimated by LDEO-HPD are within the range of the other products for F_{ant} (Figure 9A). Independent flux estimates based on interior data or atmospheric constraints also indicate consistency. Compared to F_{ANT} for 1990-1999 (Denman et al., 2007) and $F_{ANT} + F_{NAT,NS}$ 1994-2007 (Gruber, Clement, et al., 2019), all products are within the uncertainty bounds (Figure 9B).

Improved comparison to independent data in LDEO-HPD is consistent with the reduced skewness of the target variable distribution (Figure 2). Reduced skewness should particularly improve predictions at the tails of the distribution, which in this case are the decades of the 1980s and 2010s. We do not have sufficient independent data to make comparisons in the 1980s, but HPD performs best of all methods in the 2010s (Figure 7, Table 7).

Table 7. RMSE at independent datasets across decades
RMSE in each product against GLODAP and LDEO datasets across three decades: 1990s, 2000s, and 2010s. Bold values indicate the product with the lowest RMSE. LDEO values are shown in parenthesis.

	1990s	**2000s**	**2010s**
LDEO-HPD	22.0 (27.6)	**13.8** (19.0)	**15.4** (**23.4**)
SOMFFN	23.3 (28.2)	15.4 (19.9)	16.9 (26.0)
MLS	22.2 (32.7)	16.1 (25.5)	17.7 (31.6)
CMEMS	21.9 (**25.8**)	16.2 (**18.6**)	15.9 (24.8)
CSIR	**20.8** (28.4)	15.6 (21.2)	15.7 (27.9)

4 Discussion

We show that incorporating physical models into machine learning algorithms results in some improvement in predictions of surface ocean pCO_2. Using output from GOBMs as a prior guess allows us to reduce the skewness of the target variable distribution (Figure 2). Though GOBMs are imperfect representations of the real ocean (Hauck et al., 2020), this work illustrates that they can provide useful prior estimates of pCO_2 upon which data can improve using machine learning algorithms. By merging models and data,

LDEO-HPD reduces error in estimates of pCO_2 (Figure 6), with the recent decades being the most improved (Figure 7, Table 7).

The LDEO-HPD approach of correcting GOBMs additionally estimates the misfit between model output and observed pCO_2 at all points in space and time (Figure 3). These misfit fields offer potential to facilitate model development by highlighting and visualizing the times and regions where the model performs poorly.

LDEO-HPD indicates an ocean carbon sink that is on the upper end of the suite of products for 1990-1999, but at the lower end of the suite of products for 2009-2018 (Figure 9). This finding is consistent with the reduced skewness in the target variable in our approach. pCO_2 data the 1980s are extremely sparse, but in the 1990s they are almost as numerous as in the subsequent decades. The 1980s and 1990s are both skewed low with respect to the overall pCO_2 distribution due to the long-term increase of surface ocean pCO_2 in response to atmospheric pCO_2 growth. The whole pCO_2 distribution is centered somewhere between the decades the 1990s and 2000s (Figure 2A,B). Thus, pCO_2 predictions in since the 2000s in other machine learning approaches are potentially skewed slightly low, i.e. toward the mean of the overall distribution. A negative bias in ocean pCO_2 would increase the air-sea pCO_2 difference and drive a greater flux into the ocean (Equation 2). The opposite direction of skew may be occurring in the 1990s, with pCO_2 skewed slightly high and fluxes skewed low. Machine learning algorithms are based on the assumption that the training and testing data are independent and identically distributed and thus drawn from the same data generating distribution (Goodfellow et al., 2016). A tighter distribution is easier for a statistical algorithm to fit. By LDEO-HPD fitting model-data misfit, the skewness of the target variable distribution is largely eliminated (Figure 2C,D). In comparison to other products, the reduction of skewness in LDEO-HPD (Figure 2A,B) is consistent with both the improved fit to independent observations (Figure 7, Table 7), and the slightly larger ocean carbon sink LDEO-HPD in the 1990s and the slightly smaller sink since 2009 (Figure 9).

The combination of data-based machine learning with specific physical constraints or with the physics embodied in dynamical models is an emerging concept for earth science applications (Karpatne et al., 2017; Reichstein et al., 2019). As in other efforts that have corrected dynamical models using observations (Watt-Meyer et al., 2021), we use GOBMs as a prior estimate of the surface ocean pCO_2 field, and then correct these fields with data. The fact that the distribution of the target variable is substantially tightened (Figure 2A,C) illustrates that GOBMs bring valuable prior physical information to support a robust reconstruction. For example, where pCO_2 is high, such as in the equatorial Pacific, it is also high in the model; and thus model-data misfits are constrained in magnitude (Figure 2C). If the GOBMs did not provide a useful prior, i.e. had little relationship to the observations, the spread of model-data misfit would be expected to be larger than of pCO_2 alone. Tightening the distribution of the target variable supports our improved machine learning based predictions (Figure 6, 7).

Gregor et al. (2019) suggest we may have "hit a wall" in our ability to extrapolate sparse pCO_2 data to global coverage. Here, we illustrate that incorporating model output and addressing skewness of the target variable distribution allows some additional improvement in prediction skill. In addition, LDEO-HPD employs an XGB algorithm, which is also found to be promising by Gregor et al. (2019). Stamell et al. (2020) showed the XGB algorithm performs slightly better in pCO_2 extrapolation than neural network or random forest algorithms. XGB's strength is its self-correcting nature in which each additional tree improves upon errors made in the previous.

For 2009-2018, the Global Carbon Budget 2020 (Friedlingstein et al., 2020) indicates an ocean anthropogenic sink (F_{ANT}) of -2.5 $\pm$ 0.6 PgC/yr (Figure 9). LDEO-HPD indicates a similar flux, -2.6 $\pm$ 0.28 PgC/yr ($F_{ANT} = F_{NET}$ - F_{RIV}). The standard deviation across the nine error-corrected GOBMs (0.1 PgC/yr) and the uncertainty asso-

ciated with F_{RIV} (0.26 PgC/yr) are added in quadrature to produce the total uncertainty of LDEO-HPD. The other four products discussed here (Table 5) have mean uptake of -2.6 ± 0.26 to -2.8 ± 0.26 PgC/yr, using F_{RIV} = +0.49 ± 0.26 PgC/yr to calculate F_{ANT} from F_{NET} for all. Thus, all products are consistent with the GCB2020. It is important to note that our updated estimate of F_{RIV} is lower than that used by the Global Carbon Budget 2020 (+0.61 PgC/yr), and by Hauck et al. (2020) (+0.78 PgC/yr), thus reducing the apparent model to observation product discrepancy that has been previously discussed (Friedlingstein et al., 2020). In addition, the harmonized flux calculation approach used here slightly reduces ocean uptake for some products (Fay et al., 2021). In summary, for 2009-2018, we find that all products fall within the uncertainties of the GCB2020 for F_{ANT}, with LDEO-HPD on the lower end of the range and slightly closer to the GCB2020 mean.

5 Conclusions

To reconstruct the real ocean's surface ocean pCO_2, LDEO-HPD rectifies output of nine global ocean biogeochemical models (GOBMs) by learning the misfit from observed pCO_2 using an XGB algorithm and observed driver fields. LDEO-HPD improves prediction accuracy compared to other state-of-the-art pCO_2 data products, as indicated by improved fit to independent data. This suggests that GOBM output adds useful prior information to machine learning for this application. The globally and temporally complete misfits learned by the algorithm additionally have promise as a new diagnostic and visualization tool with which GOBM performance can be assessed. Adding physical information, here by using GOBMs as a prior, and addressing temporal skewness in surface ocean pCO_2 distribution offer promising directions for continued improvement in the fidelity of machine-learning based reconstructions of the ocean carbon sink. The LDEO-HPD suggests a global ocean sink for anthropogenic carbon that is within the range of the suite of existing pCO_2 observation-based products, and that is in agreement with the Global Carbon Budget 2020 (Friedlingstein et al., 2020).

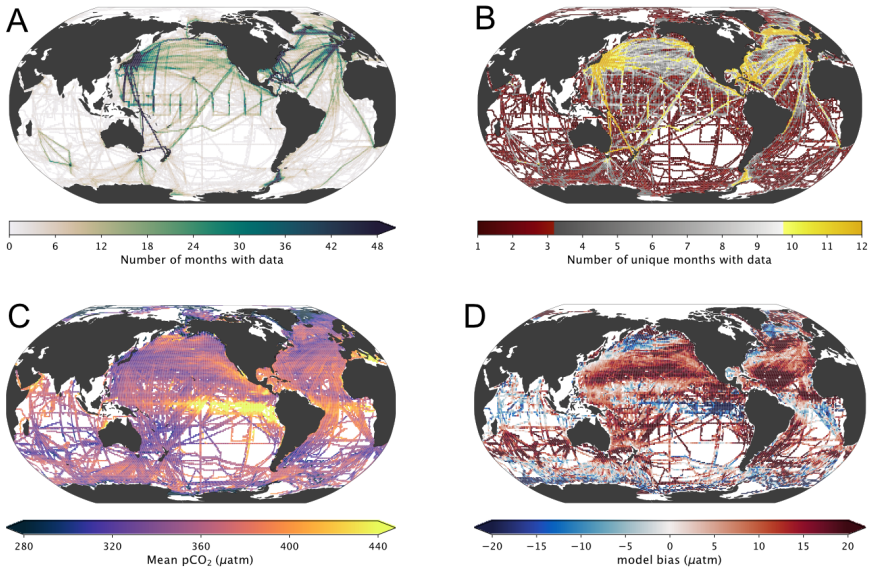

Figure 1. A) Total number of months over 1982-2018 with observations. B) Number of unique months with observations. C) Long-term mean pCO_2 at each 1°x1° pixel. D) Bias between SOCAT and mean of nine GOBMs.

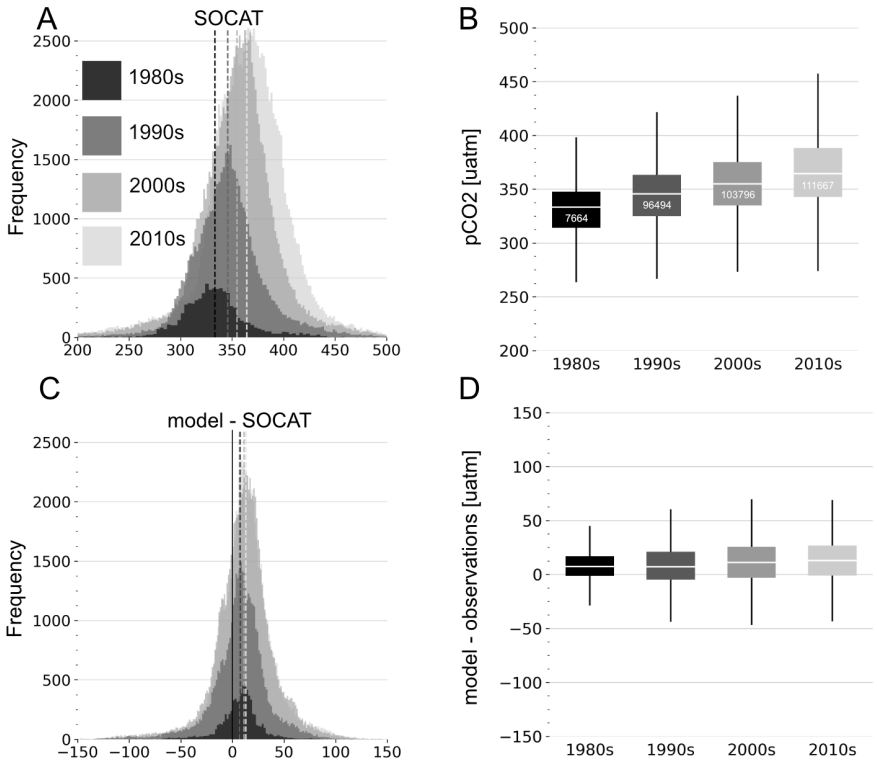

Figure 2. A) Histogram of SOCAT pCO_2 observations in 1980s, 1990s, 2000s and 2010s shown by different shades of gray. Dotted line indicates mean pCO_2. B) boxplot of observations for each decade. Whisker indicates 1.5*IQR, observations outside the whisker have been omitted. White line indicates the mean and the number inside in the box indicates the number of observations within that decade. C) Histogram of the difference between CESM model and SOCAT and D) is the corresponding boxplot. Due to different internal model structures, the long-term trend from 1980s to 2010s varies from -7 μatm to +9 μatm.

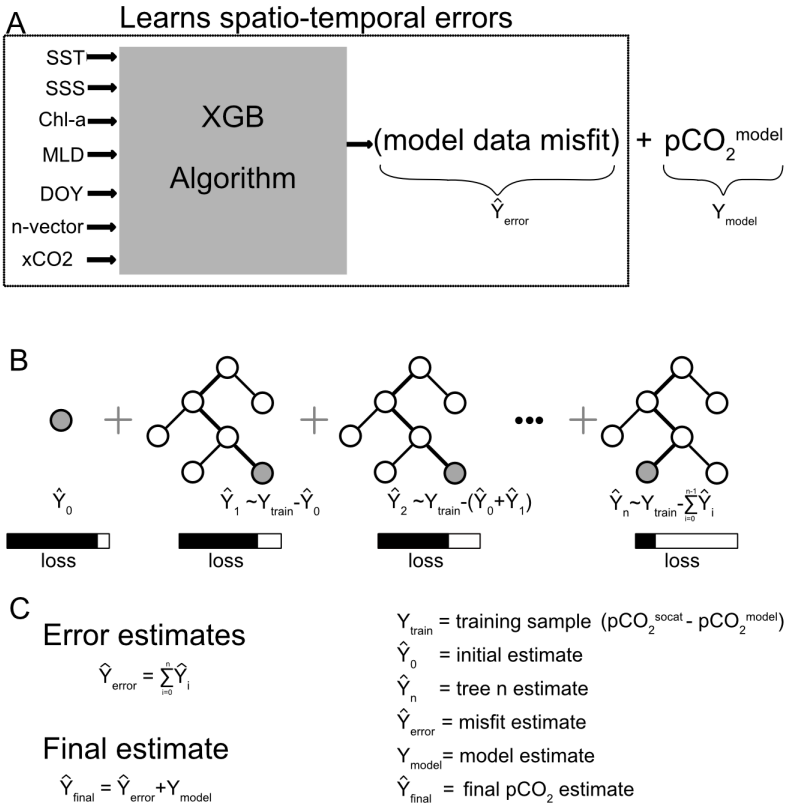

Figure 3. A) Schematic of LDEO-HPD method. A relationship between a suite of auxiliary features and the model data misfit is learned via the XGB algorithm. Spatio-temporal errors are then added back to the model's pCO_2 field to create the final product. B) outlines the XGB algorithm, where decision trees are sequentially added to improve the mistakes of the previous trees. Each additional tree reduces the loss and improves the overall performance of the algorithm. C) The final estimate of pCO_2 is the model-data misfit estimated at all global points plus the original model. This process is done independently for each of the 9 GOBMs and the final estimate is the average pCO_2.

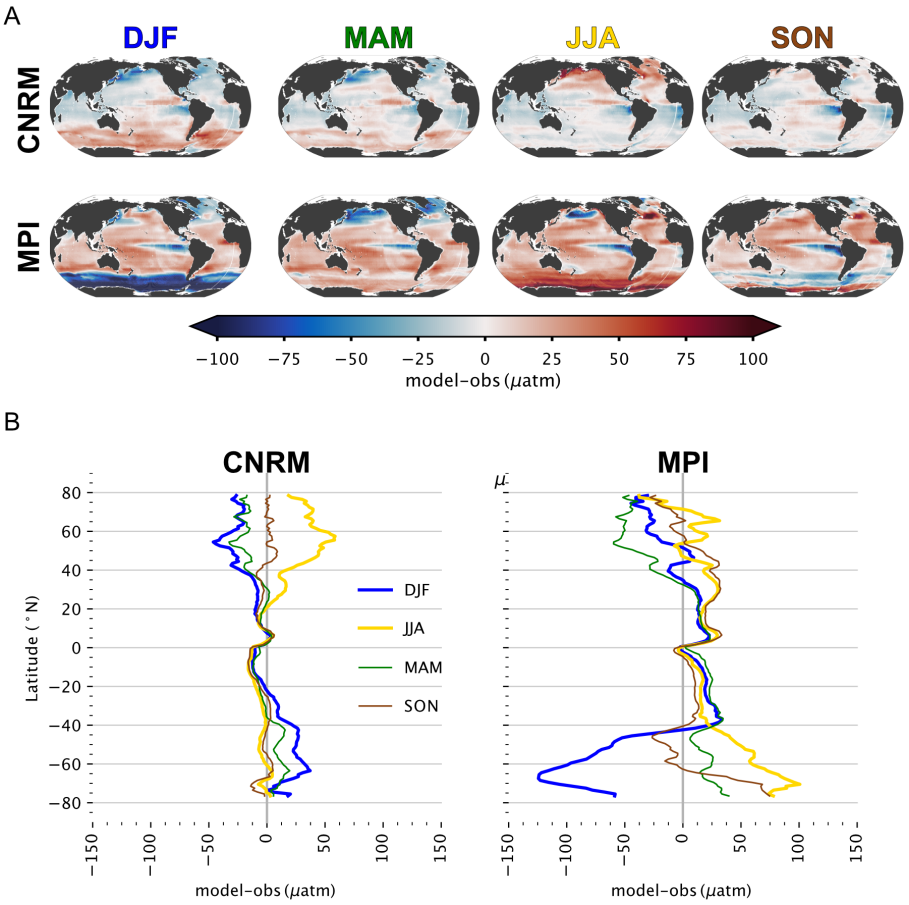

Figure 4. A) Average pCO_2 misfit in the MPI and CNRM model for all years, December, January, and February (DJF); March, April and May (MAM); June, July, and August (JJA); and September October and November (SON). B) Zonally average pCO_2 misfit in the MPI and CNRM models for DJF, JJA, MAM, and SON.

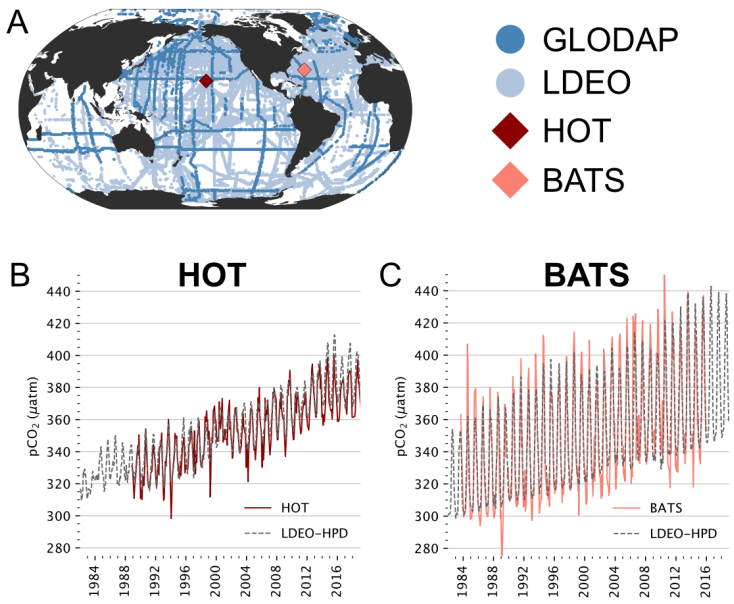

Figure 5. A) Locations of independent datasets. BATS and HOT are timeseries, while the GLODAP and LDEO are spatially varying. B) comparison of HOT with LDEO-HPD output. C) comparison between BATS and LDEO-HPD output

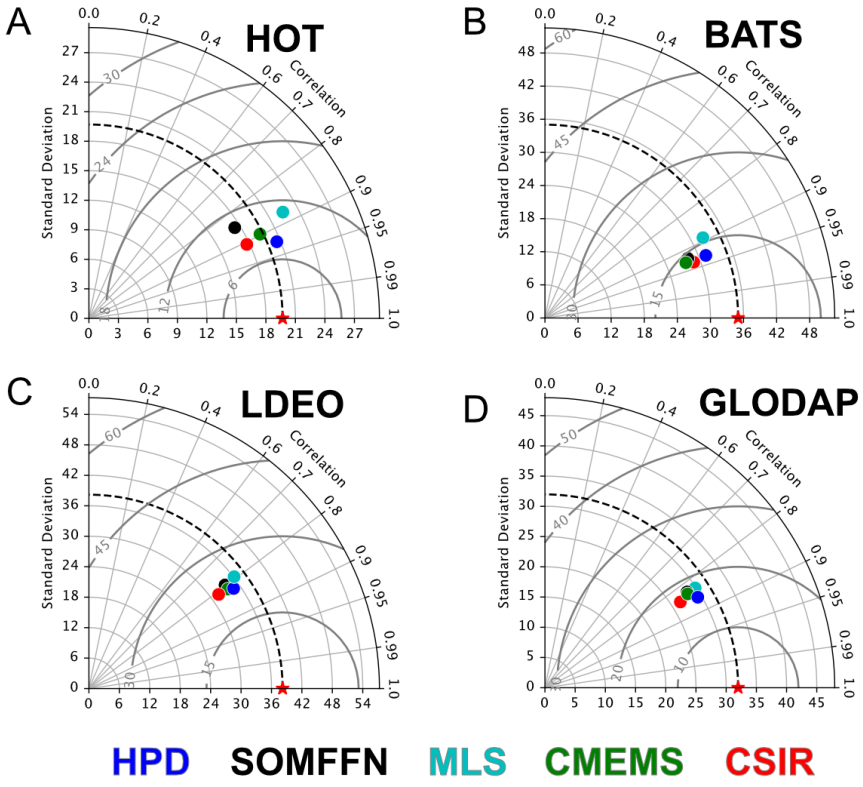

Figure 6. Taylor diagrams display the performance of published gap-filling techniques and LDEO-HPD product. Performance is evaluated at two timeseries: A) HOT and B) BATS; and two global datasets: C) LDEO and D) GLODAP. Red star indicates standard deviation of each dataset.

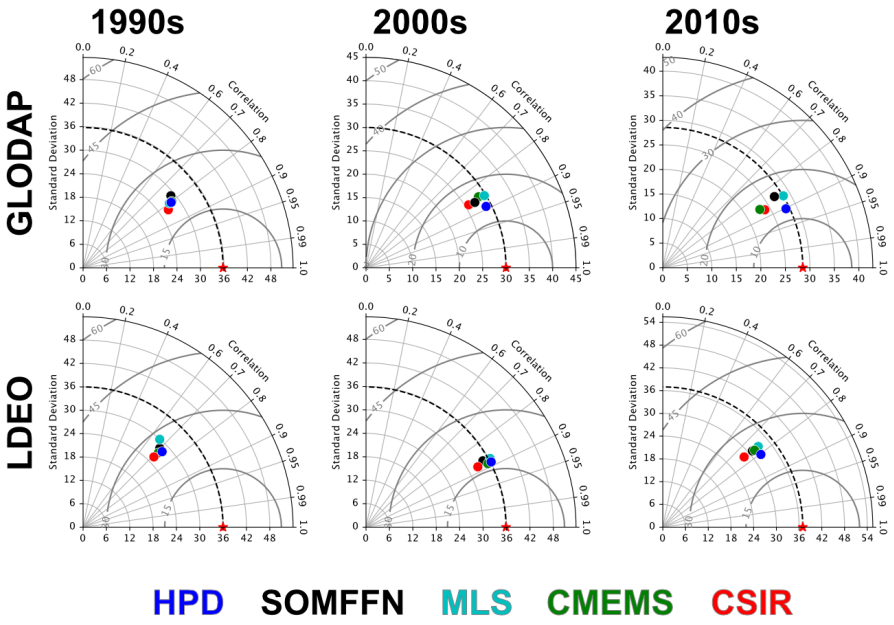

Figure 7. Taylor diagrams display the performance of published gap-filling techniques and LDEO-HPD product. Performance is evaluated at two global datasets, LDEO and GLODAP, using data in the from 1990-1999 (1990s), 2000-2009 (2000s), and 2010-2018 (2010s).Red star indicates standard deviation of each dataset.

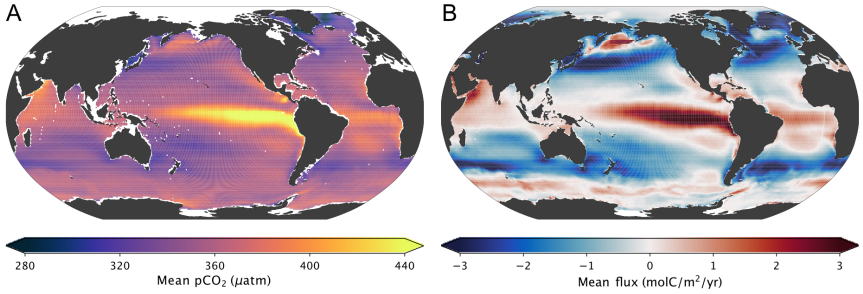

Figure 8. Mean A) pCO_2 and B) net CO_2 flux over 1982-2018 estimated from LDEO-HPD. A spatially complete map of CO_2 flux is achieved by filling in gaps with a trend plus climatology.

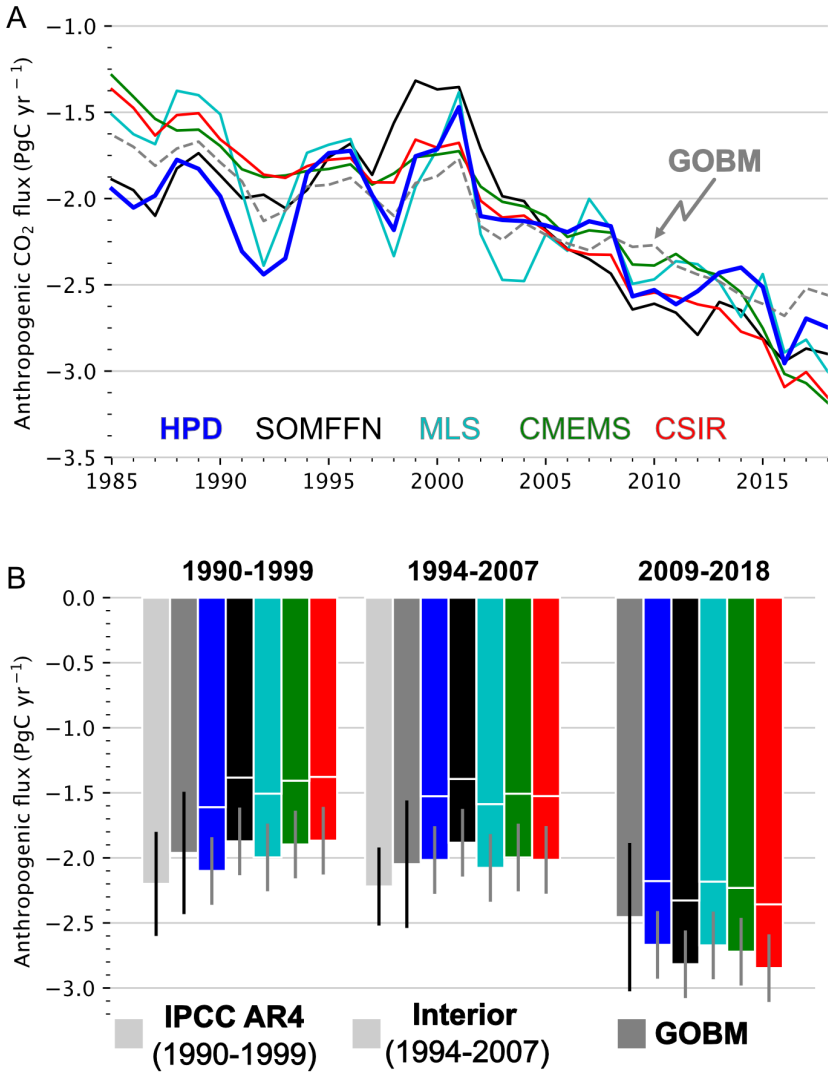

Figure 9. A) Anthropogenic air-sea CO_2 exchange (F_{ANT}) for 1985-2018 from LDEO-HPD and four other products: SOMFFN, MLS, CMEMS, CSIR-ML6. Positive is to the atmosphere. Gray dash is the mean of the 9 GOBM priors, which are also the basis for the ocean sink estimate of the Global Carbon Budget 2020 (Friedlingstein et al., 2020). B) Anthropogenic CO_2 flux for 1990-99, 1994-2007, and 2009-2018. Light gray bar indicates IPCC AR4 or interior observation-based estimates with uncertainty. Dark gray bar is the mean of the nine GOBMs. Colored bars indicate observation-based estimates. The white line separates F_{NET} from the products and F_{RIV}, estimated as the average of three estimates (0.49 PgC/yr), see section 2.8

Acknowledgments

We acknowledge support from Columbia University. M.Y acknowledges support from the Data Science Institute scholar program. The Surface Ocean CO_2 Atlas (SOCAT) is an international effort, endorsed by the International Ocean Carbon Coordination Project (IOCCP), the Surface Ocean Lower Atmosphere Study (SOLAS) and the Integrated Marine Biosphere Research (IMBeR) program, to deliver a uniformly quality-controlled surface ocean CO_2 database. The many researchers and funding agencies responsible for

the collection of data and quality control are thanked for their contributions to SOCAT. We acknowledge data were collected and made freely available by the Southern Ocean Carbon and Climate Observations and Modeling (SOCCOM) Project funded by the National Science Foundation, Division of Polar Programs (NSF PLR -1425989), supplemented by NASA, and by the International Argo Program and the NOAA programs that contribute to it. (http://www.argo.ucsd.edu, http://argo.jcommops.org). The Argo Program is part of the Global Ocean Observing System. Analysis scripts and LDEO-HPD code is available at `https://github.com/lgloege/LDEO-HPD` and LDEO-HPD output is available at `https://zenodo.org/record/4760205`.

References

Adcroft, A., Anderson, W., Balaji, V., Blanton, C., Bushuk, M., Dufour, C. O., ... others (2019). The gfdl global ocean and sea ice model om4. 0: Model description and simulation features. *Journal of Advances in Modeling Earth Systems*, *11*(10), 3167–3211.

Aumont, O., Éthé, C., Tagliabue, A., Bopp, L., & Gehlen, M. (2015). Pisces-v2: an ocean biogeochemical model for carbon and ecosystem studies. *Geoscientific Model Development Discussions*, *8*(2).

Aumont, O., Orr, J. C., Monfray, P., Ludwig, W., Amiotte Suchet, P., & Probst, J. L. (2001, June). Riverine-driven interhemispheric transport of carbon. *Global Biogeochem. ...*, *15*, 393–405.

Bakker, D. C. E., Pfeil, B., Landa, C. S., Metzl, N., O'Brien, K. M., Olsen, A., ... Xu, S. (2016). A multi-decade record of high-quality fco_2 data in version 3 of the surface ocean co_2 atlas (socat). *Earth System Science Data*, *8*(2), 383–413. Retrieved from `https://www.earth-syst-sci-data.net/8/383/2016/` doi: 10.5194/essd-8-383-2016

Bates, N. R. (2007). Interannual variability of the oceanic co2 sink in the subtropical gyre of the north atlantic ocean over the last 2 decades. *Journal of Geophysical Research: Oceans*, *112*(C9).

Berthet, S., Séférian, R., Bricaud, C., Chevallier, M., Voldoire, A., & Ethé, C. (2019). Evaluation of an online grid-coarsening algorithm in a global eddy-admitting ocean biogeochemical model. *Journal of Advances in Modeling Earth Systems*, *11*(6), 1759–1783.

Bockmon, E. E., & Dickson, A. G. (2015). An inter-laboratory comparison assessing the quality of seawater carbon dioxide measurements. *Marine Chemistry*, *171*, 36–43.

Buitenhuis, E. T., Hashioka, T., & Quéré, C. L. (2013). Combined constraints on global ocean primary production using observations and models. *Global Biogeochemical Cycles*, *27*(3), 847–858.

Chen, T., & Guestrin, C. (2016). Xgboost: A scalable tree boosting system. In *Proceedings of the 22nd acm sigkdd international conference on knowledge discovery and data mining* (pp. 785–794).

Denman, K. L., Brasseur, G. P., Chidthaisong, A., Ciais, P., Cox, P. M., Dickinson, R. E., ... Steffen, W. (2007). Couplings between changes in the climate system and biogeochemistry. In *Climate change 2007: The physical science basis* (p. 499-588). United States: Cambridge University Press.

Denvil-Sommer, A., Gehlen, M., Vrac, M., & Mejia, C. (2019). Lsce-ffnn-v1: a two-step neural network model for the reconstruction of surface ocean pco_2 over the global ocean. *Geoscientific Model Development*, *12*(5), 2091–2105. Retrieved from `https://www.geosci-model-dev.net/12/2091/2019/` doi: 10.5194/gmd-12-2091-2019

Dickson, A. G., Sabine, C. L., & Christian, J. R. (2007). *Guide to best practices for ocean co2 measurements.* North Pacific Marine Science Organization.

Doney, S. C., Lima, I., Feely, R. A., Glover, D. M., Lindsay, K., Mahowald, N., ...

Wanninkhof, R. (2009). Mechanisms governing interannual variability in upper-ocean inorganic carbon system and air–sea co2 fluxes: Physical climate and atmospheric dust. *Deep Sea Research Part II: Topical Studies in Oceanography*, *56*(8-10), 640–655.

Dore, J. E., Lukas, R., Sadler, D. W., Church, M. J., & Karl, D. M. (2009). Physical and biogeochemical modulation of ocean acidification in the central north pacific. *Proceedings of the National Academy of Sciences*, *106*(30), 12235–12240.

Fay, A., Gregor, L., Landschützer, P., McKinley, G. A., Gruber, N., Gehlen, M., ... Zeng, J. (2021). Harmonization of global surface ocean pCO_2 mapped products and their flux calculations; an improved estimate of the ocean carbon sink. *Earth System Science Data*, *submitted*.

Friedlingstein, P., Jones, M. W., O'Sullivan, M., Andrew, R. M., Hauck, J., Peters, G. P., ... Zaehle, S. (2019). Global Carbon Budget 2019. *Earth System Science Data*, *11*(4), 1783–1838.

Friedlingstein, P., O'Sullivan, M., Jones, M. W., Andrew, R. M., Hauck, J., Olsen, A., ... others (2020). Global carbon budget 2020. *Earth System Science Data*, *12*(4), 3269–3340.

Gade, K. (2010). A non-singular horizontal position representation. *The journal of navigation*, *63*(3), 395–417.

Gloege, L., McKinley, G., Landschützer, P., Fay, A., Frölicher, T., Fyfe, J., ... others (2021). Quantifying errors in observationally-based estimates of ocean carbon sink variability. *GBC (in press)*.

Goodfellow, I., Bengio, Y., & Courville, A. (2016). *Deep learning*. MIT Press. (`http://www.deeplearningbook.org`)

Gregor, L., & Gruber, N. (2021, March). OceanSODA-ETHZ: a global gridded data set of the surface ocean carbonate system for seasonal to decadal studies of ocean acidification. *Earth System Science Data*, 1–32. doi: 10.5194/essd-13-777-2021

Gregor, L., Kok, S., & Monteiro, P. (2017). Empirical methods for the estimation of southern ocean co 2: support vector and random forest regression. *Biogeosciences*, *14*(23), 5551–5569.

Gregor, L., Lebehot, A. D., Kok, S., & Scheel Monteiro, P. M. (2019). A comparative assessment of the uncertainties of global surface ocean CO_2 estimates using a machine-learning ensemble (CSIR-ML6 version 2019a)–have we hit the wall? *Geoscientific Model Development*, *12*(12), 5113–5136.

Gruber, N., Clement, D., Carter, B. R., Feely, R. A., Van Heuven, S., Hoppema, M., ... Wanninkhof, R. (2019, March). The oceanic sink for anthropogenic CO_2 from 1994 to 2007. *Science*, *363*(6432), 1193–1199.

Gruber, N., Landschützer, P., & Lovenduski, N. S. (2019). The variable Southern Ocean carbon sink. *Annual Review of Marine Science*, *11*, 159–186.

Hain, M. P., Sigman, D. M., Higgins, J. A., & Haug, G. H. (2015). The effects of secular calcium and magnesium concentration changes on the thermodynamics of seawater acid/base chemistry: Implications for eocene and cretaceous ocean carbon chemistry and buffering. *Global Biogeochemical Cycles*, *29*(5), 517–533.

Harada, Y., Kamahori, H., Kobayashi, C., Endo, H., Kobayashi, S., Ota, Y., ... Takahashi, K. (2016). The jra-55 reanalysis: Representation of atmospheric circulation and climate variability. *Journal of the Meteorological Society of Japan. Ser. II*, *94*(3), 269–302.

Hauck, J., Zeising, M., Le Quéré, C., Gruber, N., Bakker, D. C. E., Bopp, L., ... Séférian, R. (2020, October). Consistency and challenges in the ocean carbon sink estimate for the Global Carbon Budget . *Frontiers in Marine Science*, *7*, 3167.

Hersbach, H., Bell, B., Berrisford, P., Hirahara, S., Horányi, A., Muñoz-Sabater, J., ... others (2020). The era5 global reanalysis. *Quarterly Journal of the Royal*

Meteorological Society, *146*(730), 1999–2049.

Jacobson, A. R., Mikaloff Fletcher, S. E., Gruber, N., Sarmiento, J. L., & Gloor, M. (2007, March). A joint atmosphere-ocean inversion for surface fluxes of carbon dioxide: 1. Methods and global-scale fluxes. *Global Biogeochemical Cycles*, *21*(1), 273.

Karpatne, A., Watkins, W., Read, J., & Kumar, V. (2017). Physics-guided neural networks (pgnn): An application in lake temperature modeling. *arXiv preprint arXiv:1710.11431*.

Lacroix, F., Ilyina, T., & Hartmann, J. (2020). Oceanic co 2 outgassing and biological production hotspots induced by pre-industrial river loads of nutrients and carbon in a global modeling approach. *Biogeosciences*, *17*(1), 55–88.

Landschützer, P., Gruber, N., Bakker, D., & Schuster, U. (2014). Recent variability of the global ocean carbon sink. *Global Biogeochemical Cycles*, *28*(9), 927–949.

Landschützer, P., Gruber, N., & Bakker, D. C. (2016). Decadal variations and trends of the global ocean carbon sink. *Global Biogeochemical Cycles*, *30*(10), 1396–1417.

Landschützer, P., Gruber, N., & Bakker, D. C. (2020). *An observation-based global monthly gridded sea surface pco2 product from 1982 onward and its monthly climatology (ncei accession 0160558). version 5.5. noaa national centers for environmental information.* Retrieved from `https://www.ncei.noaa.gov/access/ocean-carbon-data-system/oceans/SPCO2_1982_present_ETH_SOM_FFN.html` doi: doi.org/10.7289/V5Z899N6

Landschützer, P., Laruelle, G. G., Roobaert, A., & Regnier, P. (2020, May). A uniform pCO_2 climatology combining open and coastal oceans . *Earth System Science Data*, 1–30.

Law, R. M., Ziehn, T., Matear, R. J., Lenton, A., Chamberlain, M. A., Stevens, L. E., ... others (2017). The carbon cycle in the australian community climate and earth system simulator (access-esm1)–part 1: Model description and pre-industrial simulation. *Geoscientific Model Development*, *10*(7), 2567.

Le Quéré, C., Raupach, M. R., Canadell, J. G., Marland, G., Bopp, L., Ciais, P., ... others (2009). Trends in the sources and sinks of carbon dioxide. *Nature geoscience*, *2*(12), 831–836.

Lueker, T. J., Dickson, A. G., & Keeling, C. D. (2000). Ocean pco2 calculated from dissolved inorganic carbon, alkalinity, and equations for k1 and k2: validation based on laboratory measurements of co2 in gas and seawater at equilibrium. *Marine chemistry*, *70*(1-3), 105–119.

McKinley, G. A., Fay, A. R., Eddebbar, Y. A., Gloege, L., & Lovenduski, N. S. (2020, June). External Forcing Explains Recent Decadal Variability of the Ocean Carbon Sink. *AGU Advances*, *1*(2), 1.

McKinley, G. A., Pilcher, D. J., Fay, A. R., Lindsay, K., Long, M. C., & Lovenduski, N. S. (2016, February). Timescales for detection of trends in the ocean carbon sink. *Nature*, *530*(7591), 469–472.

Mears, C. A., Scott, J., Wentz, F. J., Ricciardulli, L., Leidner, S. M., Hoffman, R., & Atlas, R. (2019). A near-real-time version of the cross-calibrated multiplatform (ccmp) ocean surface wind velocity data set. *Journal of Geophysical Research: Oceans*, *124*(10), 6997–7010.

Orr, J. C., Najjar, R. G., Aumont, O., Bopp, L., Bullister, J. L., Danabasoglu, G., ... others (2017). Biogeochemical protocols and diagnostics for the cmip6 ocean model intercomparison project (omip). *Geoscientific Model Development*, *10*(6), 2169–2199.

Paulsen, H., Ilyina, T., Six, K. D., & Stemmler, I. (2017). Incorporating a prognostic representation of marine nitrogen fixers into the global ocean biogeochemical model hamocc. *Journal of Advances in Modeling Earth Systems*, *9*(1), 438–464.

Peters, G. P., Le Quéré, C., Andrew, R. M., Canadell, J. G., Friedlingstein, P., Ilyina, T., ... Tans, P. (2017). Towards real-time verification of CO2 emissions. *Nature Climate Change*, *7*(12), 848–850.

Raupach, M. R., Gloor, M., Sarmiento, J. L., Canadell, J. G., Frolicher, T. L., Gasser, T., ... Trudinger, C. M. (2014). The declining uptake rate of atmospheric CO_2 by land and ocean sinks. *Biogeosciences*, *11*(13), 3453–3475.

Reichstein, M., Camps-Valls, G., Stevens, B., Jung, M., Denzler, J., Carvalhais, N., et al. (2019). Deep learning and process understanding for data-driven earth system science. *Nature*, *566*(7743), 195.

Resplandy, L., Keeling, R., Rödenbeck, C., Stephens, B., Khatiwala, S., Rodgers, K., ... Tans, P. (2018). Revision of global carbon fluxes based on a reassessment of oceanic and riverine carbon transport. *Nature Geoscience*, *11*(7), 504–509.

Ridge, S., & McKinley, G. A. (2020). Ocean carbon uptake under aggressive emission mitigation. *Biogeosciences Discussions*. doi: 10.5194/bg-2020-254

Rödenbeck, C., Bakker, D., Metzl, N., Olsen, A., Sabine, C., Cassar, N., ... Heimann, M. (2014). Interannual sea–air co 2 flux variability from an observation-driven ocean mixed-layer scheme. *Biogeosciences*, *11*(17), 4599–4613.

Rödenbeck, C., Bakker, D. C., Gruber, N., Iida, Y., Jacobson, A. R., Jones, S., ... others (2015). Data-based estimates of the ocean carbon sink variability–first results of the surface ocean pco2 mapping intercomparison (socom). *Biogeosciences*, *12*, 7251–7278.

Roobaert, A., Laruelle, G. G., Landschützer, P., Gruber, N., Chou, L., & Regnier, P. (2019, December). The Spatiotemporal Dynamics of the Sources and Sinks of CO2 in the Global Coastal Ocean. *Global Biogeochemical Cycles*, *33*(12), 1693–1714. doi: 10.1016/j.polar.2016.03.006

Sabine, C. L., Hankin, S., Koyuk, H., Bakker, D. C. E., Pfeil, B., Olsen, A., ... Yoshikawa-Inoue, H. (2013). Surface ocean co_2 atlas (socat) gridded data products. *Earth System Science Data*, *5*(1), 145–153. Retrieved from `https://www.earth-syst-sci-data.net/5/145/2013/` doi: 10.5194/essd-5-145-2013

Sasse, T., McNeil, B., & Abramowitz, G. (2013). A novel method for diagnosing seasonal to inter-annual surface ocean carbon dynamics from bottle data using neural networks. *Biogeosciences*, *10*(6), 4319–4340.

Schwinger, J., Goris, N., Tjiputra, J. F., Kriest, I., Bentsen, M., Bethke, I., ... Heinze, C. (2016). Evaluation of noresm-oc (versions 1 and 1.2), the ocean carbon-cycle stand-alone configuration of the norwegian earth system model (noresm1). *Geoscientific Model Development*, *9*, 2589–2622.

Stamell, J., Rustagi, R. R., Gloege, L., & McKinley, G. A. (2020). Strengths and weaknesses of three machine learning methods for pco 2 interpolation. *Geoscientific Model Development Discussions*, 1–25.

Stow, C. A., Jolliff, J., McGillicuddy Jr, D. J., Doney, S. C., Allen, J. I., Friedrichs, M. A., ... Wallhead, P. (2009). Skill assessment for coupled biological/physical models of marine systems. *Journal of Marine Systems*, *76*(1-2), 4–15.

Takahashi, T., Sutherland, S. C., & Kozyr, A. (2019). Global ocean surface water partial pressure of co2 database: measurments performed during 1957–2018 (version 2018).

Taylor, K. E. (2001). Summarizing multiple aspects of model performance in a single diagram. *Journal of Geophysical Research: Atmospheres*, *106*(D7), 7183–7192.

Tjiputra, J. F., Olsen, A., Bopp, L., Lenton, A., Pfeil, B., Roy, T., ... Heinze, C. (2014). Long-term surface pco2 trends from observations and models. *Tellus B: Chemical and Physical Meteorology*, *66*(1), 23083.

Wanninkhof, R. (1992). Relationship between wind speed and gas exchange over the ocean. *Journal of Geophysical Research: Oceans*, *97*(C5), 7373–7382.

Wanninkhof, R. (2014). Relationship between wind speed and gas exchange over the

ocean revisited. *Limnology and Oceanography: Methods*, *12*(6), 351–362.

Watson, A. J., Schuster, U., Shutler, J. D., Holding, T., Ashton, I. G. C., Landschützer, P., ... Goddijn-Murphy, L. (2020, August). Revised estimates of ocean-atmosphere CO_2 flux are consistent with ocean carbon inventory. *Nature Communications*, 1–6.

Watt-Meyer, O., Brenowitz, N., Clark, S. K., Henn, B., Kwa, A., McGibbon, J., ... Bretherton, C. (2021, January). Correcting weather and climate models by machine learning nudged historical simulations. , 1–13. doi: 10.1002/essoar.10505959.1

Weiss, R. (1974). Carbon dioxide in water and seawater: the solubility of a non-ideal gas. *Marine chemistry*, *2*(3), 203–215.